








802 Gbps Coherent Transmission With a Silicon Ring Resonator Coupling-Modulation-Based Dual-Polarization I/Q Modulator

X. Chen , A. Mistry, M. Bahadori, K. Padmaraju, M. Malinowski, D. Che , R. Sukkar, R. Younce, A. Horth, Y. Dziashko, H. Guan, R. Shi , D. Gill, A. Seyoum, J. Naik , D. Lim, A. El Sayed, A. Rylyakov, M. Schmidt, Z. Luo , R. Patel , P. Magill, G. Burrell, J. Basak, D. Chapman, A. Mikami, Y. Man, M. Astolfi , A. Leven, and N. A. F. Jaeger

(Top-Scored Paper)

Abstract—In this paper, we present a high-speed, small form-factor, C-band, dual-polarization I/Q modulator for coherent transmission. The silicon ring-resonator-based modulator, based on coupling modulation via a traveling-wave Mach-Zehnder modulator, is co-packaged with SiGe drivers. We demonstrate an 802.6 Gbps net data rate transmission via 78-km standard single-mode fiber with 90-GBaud probabilistically shaped (PS)-64-QAM modulation.

Index Terms—Coherent transmission, fiber transmission, high-speed optical transceivers, resonant modulator, silicon photonics.

I. INTRODUCTION

THE large discrepancy between the net annual traffic growth rate (40% ~ 60%), and the data rate growth rate per coherent module (~20%) will most likely push future optical transceivers towards higher levels of parallelization and integration [1], [2]. It is expected that tens of parallel spatial channels using multiple transceiver systems, integrated into a single module, will be required to form an interface to fulfill this traffic growth [1]. To reliably enable this high level of compact integration, adopting transceiver technologies that maintain compact form-factors, high yield, and high performance is paramount. Silicon photonics (SiPh) has been widely demonstrated as a promising technology for this applications

space due to its stable performance, high yields, and small device footprints [3], [4], [5]. Commercial SiPh-based transceivers are widely available on the open market [6], [7], [8]. In a SiPh technology platform, a wide variety of compact components have been demonstrated, that occupy less than a few tens of μm^2 of space, such as photodiodes, power splitters/combiners, and attenuators. However, electro-optic modulators used in high-speed coherent transceivers are almost exclusively made in the form of large footprint travelling-wave Mach-Zehnder modulators (TW-MZMs). By design, TW-MZMs require a certain length to achieve an acceptable modulation depth [9], [10], with typical lengths of the TW-MZMs on SiPh platform ranging from 4 to 7 mm. Four MZMs are needed to form one dual-polarization (DP) I/Q modulator for a coherent transmitter, and hence, the typical size of a SiPh-based DP I/Q modulator often approaches $\sim 30 \text{ mm}^2$. Given that all other components are on the order of tens of μm^2 , the modulator is often the device that occupies most of the area on the photonic integrated circuit (PIC) used in a SiPh-based transceiver. Similarly, in other material systems (e.g., indium phosphide), modulators are still often the single largest component on the coherent transceiver's PIC. Thus, reducing the footprint of the electro-optic modulators can result in a significant reduction in PIC and transceiver sizes, regardless of the material, resulting in more available real-estate in optical modules to enable the forementioned higher levels of integration and parallelization.

The miniaturization of traveling-wave modulators is not a trivial task. There is a fundamental tradeoff between the length of the modulator and the required drive voltage, V_π . Often, the shorter the electrode/modulator, the higher the electro-optic 3 dB bandwidth, but the higher the V_π . Limited by the output voltage of CMOS ($\sim 0.5\text{-V}$ peak-to-peak voltage (V_{pp})) and the output voltage of broadband linear RF amplifiers ($2\text{-}\sim 4\text{-V}$ V_{pp}), SiPh-based TW-MZMs demonstrated in the literature need to approach $\sim 6\text{-mm}$ in length to have adequate V_π values that achieve bit-error ratio (BER) /optical signal-to-noise ratio (OSNR) penalties that can be handled by modern DSPs for a given net data rate [11]. Maintaining the current structure of the

Manuscript received 24 January 2024; revised 1 April 2024; accepted 17 April 2024. Date of publication 23 April 2024; date of current version 27 June 2024. (X. Chen and A. Mistry contributed equally to this work.) (Corresponding authors: Xi Chen; Ajay Mistry.)

X. Chen and D. Che are with Nokia Bell Labs, Murray Hill, NJ 07974 USA (e-mail: x.v.chen@nokia-bell-labs.com).

A. Mistry, M. Bahadori, K. Padmaraju, M. Malinowski, R. Sukkar, R. Younce, A. Horth, Y. Dziashko, H. Guan, R. Shi, D. Gill, A. Seyoum, J. Naik, D. Lim, A. El Sayed, A. Rylyakov, M. Schmidt, Z. Luo, R. Patel, P. Magill, G. Burrell, J. Basak, D. Chapman, A. Mikami, Y. Man, M. Astolfi, and A. Leven are with Nokia Advanced Optics New York, NY 10016 USA (e-mail: ajay.mistry@nokia.com).

N. A. F. Jaeger is with the Department of Electrical and Computer Engineering, University of British Columbia, Vancouver, BC V6T1Z4, Canada.

Color versions of one or more figures in this article are available at <https://doi.org/10.1109/JLT.2024.3392033>.

Digital Object Identifier 10.1109/JLT.2024.3392033

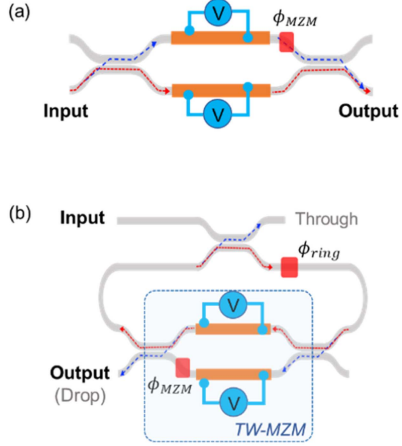


Fig. 1. Schematic diagram of: (a) a conventional traveling-wave Mach-Zehnder modulator (TW-MZM) and (b) a coupling-modulated ring resonator modulator (CMRRM).

modulator and solely relying on reducing the length to achieve a smaller modulator would result in impractically high V_π values. This necessitates a change in modulator architecture. Resonant modulators are one of the well-discussed methods to reduce the size of modulators. Common approaches include conventional ring resonators, ring-assisted MZMs, Fabry-Perot modulators, and coupling-modulated ring resonators [12], [13], [14].

Here, we demonstrate coupling-modulated ring resonator modulators (CMRRMs) for coherent modulation in the C-band, which have compact sizes, low chirp, linear transfer functions, and comparable bandwidths to TW-MZMs. We extend our paper from [15], explaining the details of the CMRR-based IQ modulators, and supplement with additional measurements and discussions. Our modulator PIC is flip-chipped onto a ball grid array (BGA) based coherent optical sub-assembly (COSA) with co-packaged SiGe RF drivers. We demonstrate 90-Gbaud DP probabilistically-shaped (PS)-64-QAM coherent transmission, supporting a net data rate of 838.6 Gbps at back-to-back (B2B) and 802.6 Gbps with 78-km standard single mode fiber (SSMF) transmission. Note the ‘net data rate’ is the information rate. We choose not to focus on the line rate in this paper, as line rate is not always a well-defined metric in modern communication systems, where probabilistic shaping and advanced error correction schemes are adopted. (More discussion on this can be found in [16]).

II. THE SILICON RING RESONATOR COUPLING BASED MODULATOR

A block diagram of our CMRRM is shown in Fig. 1(b), in comparison with a conventional TW-MZM in Fig. 1(a). The CMRRM consists of an optical cavity, with a fixed through-port directional coupler and a TW-MZM embedded in the drop-port of the cavity. The cavity has an embedded thermal phase tuner for cavity resonance locking (ϕ_{ring}), and a thermal phase tuner in the TW-MZM to set the modulator operating bias point (ϕ_{MZM}). In the CMRR modulator, the embedded TW-MZM modulates the effective drop-port coupling coefficient of the cavity; hence,

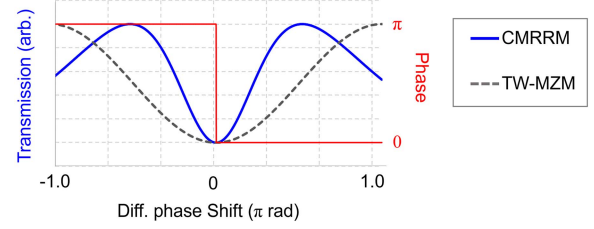


Fig. 2. Simulated transfer functions of a CMRRM and a conventional TW-MZM, at the null-bias operating condition.

the TW-MZM modulates both the output power and phase at the drop-port of the device. The embedded TW-MZM effectively gates the intracavity optical field as it exits the cavity, while the cavity itself remains fixed at resonance. Because the intracavity parameters remain fixed, when the phase shifter is driven differentially, the modulator is typically not limited by the photon lifetime of the cavity (i.e., optical linewidth), but rather by the EO bandwidth of the TW-MZM itself [14].

Fig. 2 shows the amplitude transfer function at the drop-port of a CMRRM when the device is biased at the null operating condition for coherent modulation ($\phi_{MZM} = \pi$). The transfer function has a similar sinusoidal-like shape to that of a conventional Mach-Zehnder interferometer (MZI), with the same binary phase transition across the ‘null’ operating point. The transfer function is also linear across the null operating point. Compared to the transfer function of a conventional MZI, the maximum transmission of the CMRRM occurs at an applied differential phase shift less than π . This is because, in the optical cavity, the magnitude of the circulating field is much larger than the modulator input field. The cavities have high-quality factors (Q-factors), thus very small changes in the drop-port coupling allow for large swings in the optical power coupled out of the cavity while the rest of the power is recirculated. The small change in the drop-port coupling is achieved with a proportionally small differential phase shift in the TW-MZM and, therefore, full on-to-off (or null-to-maximum) transmission swings can be achieved with a phase shift that is less than π radians. As a result, this effectively reduces the CMRRM’s equivalent V_π as compared to conventional TW-MZMs which require a π radian phase shift to achieve the full transmission swings (see Fig. 2 below).

The amount of V_π reduction depends on the Q-factor of the optical cavity. A simulated example of the V_π reduction, as a function of cavity Q-factors, is shown in Fig. 3 (here, the Q-factor, for a given cavity design, is varied by arbitrarily adjusting the round-trip loss of the cavity). As seen, the effective phase shift required to achieve a full transmission swing ($\varphi_{\pi\text{eff}}$) reduces with increasing Q-factor. For CMRRMs, because the required phase shifts in the TW-MZM are small, short EO interaction lengths are possible with the ‘reduced’ V_π s, and the overall device footprint can remain compact, and high-bandwidth TW-MZMs can be embedded in the cavity. Here, we define the CMRRM V_π reduction factor as $\varphi_{\pi\text{eff}}/\pi$ and plot it as a function of cavity Q-factor. We show in Fig. 3(b) that CMRRM can overcome the conventional V_π/BW trade-off

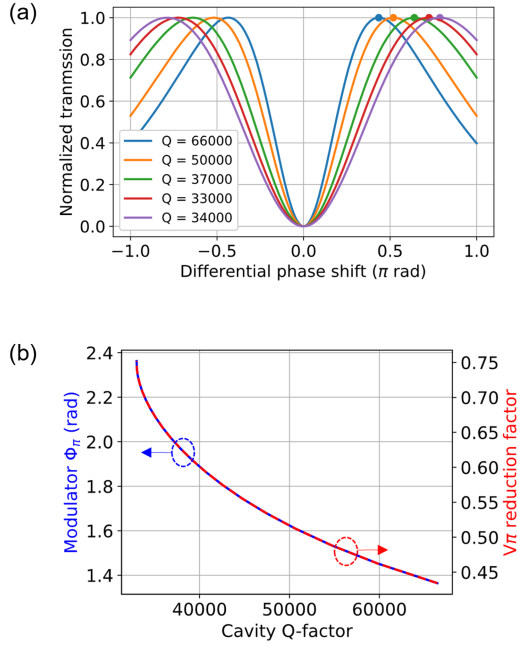


Fig. 3. (a) Simulated normalized transfer functions of CMRRMs with various cavity Q-factors and (b) CMRRM $\varphi_{\pi\text{eff}}$ and V_{π} reduction factor, as a function of the cavity Q-factor.

in conventional TW-MZM devices. For a standalone TW-MZM with a given bandwidth and V_{π} , a CMRRM with an embedded equivalent TW-MZM will have the same bandwidth, but will have a reduced V_{π} scaled by the Q-dependent V_{π} reduction factor (i.e., $V_{\pi,\text{CMRRM}} = V_{\pi,\text{TW-MZM}} \cdot \varphi_{\pi\text{eff}} / \pi$).

III. THE FABRICATED DUAL-POL I/Q MODULATOR AND THE INTEGRATED COHERENT TRANSMITTER

We designed our CMRR modulator with an electrode length of ~ 0.6 mm. Note, that this is a very short electrode for a silicon modulator, a typical length would be $5 \sim 6$ mm. For comparison purposes, a standalone SiPh TW-MZM with a 0.6 mm long electrode was fabricated on the same chip as our experimental CMRRMs and had a measured V_{π} of ~ 28 V. For the CMRRM structures with 0.6 mm long electrodes, the measured V_{π} was ~ 14 V, hence, the V_{π} reduction factor is ~ 0.5 . This is still a fairly high V_{π} (a more desirable V_{π} would be 6 V or less). We expect the V_{π} to be reduced in future designs by further optimizing the resonator Q-factor as well as improving the pn-junction and electrode designs.

To characterize the DC EO transfer function of a CMRRM, a tunable laser was input to the device at wafer level via on-PIC grating couplers, and the bias voltage of the thermal phase shifter, embedded in the TW-MZM, was swept across its operating range. The results are shown in Fig. 4(a). Good agreement is seen between our analytical model transfer function and our measured transfer function. The thru-port coupling coefficient of the CMRRM is designed such that the modulation loss at the maximum projected driver output voltage is minimized. A full model of the fabricated CMRRM can be created after the coupling coefficient and cavity loss are extracted from the DC

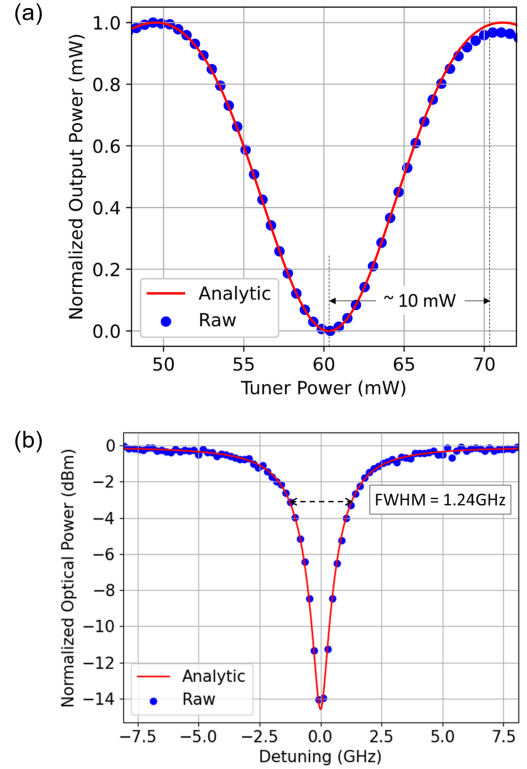


Fig. 4. (a) Measured DC transfer function of the CMRRM modulator and (b) through-port optical spectrum of the CMRR modulator when biased at null. The resonator Q-factor (~ 78000) at 1550 nm is extracted from the FWHM.

EO transfer function and after determining the DC phase efficiency of the embedded TW-MZM using that of the standalone TW-MZM test structure on the chip. The reported V_{π} value of the fabricated devices was obtained from the extracted CMRR-modulator model. The thermal tuner phase shift efficiency was 20 mW/ π and the extracted V_{π} of the standalone TW-MZM was 28 V. In Fig. 4(a), we show that the maximum transmission peak is achieved when 10 mW of power is applied to the thermal tuner in the CMRRM, yielding the V_{π} reduction factor of ~ 0.5 . In Fig. 4(b), we show the through-port optical spectrum of the CMRRM modulator when biased at the null operating point. From the optical spectrum, we extracted the full width at half maximum (FWHM) to calculate the resonator Q-factor ($\sim 78,000$) at 1550 nm. Good agreement is also shown between our measurements and our analytic model.

Fig. 5(a) shows a micrograph of a single fabricated CMRRM test structure on a bare die. Including the ring structure, the modulator occupies less than $1 \text{ mm} \times 0.3 \text{ mm}$. Four CMRRMs were arranged into a DP I/Q modulator configuration on a single silicon PIC. A micrograph of the PIC is shown in Fig. 5(b). The PIC is flip-chip packaged onto an organic substrate with flip-chip in-house-designed, high-speed, SiGe RF drivers. SSMFs were attached to the edge of the PIC on the BGA-based COSA for optical I/O.

The small-signal EO response of a standalone CMRRM test structure, measured at the wafer level, is shown in blue in Fig. 6. The measurement was taken with the TW-MZM slightly detuned from the null-bias, and with the cavity assumed to be detuned

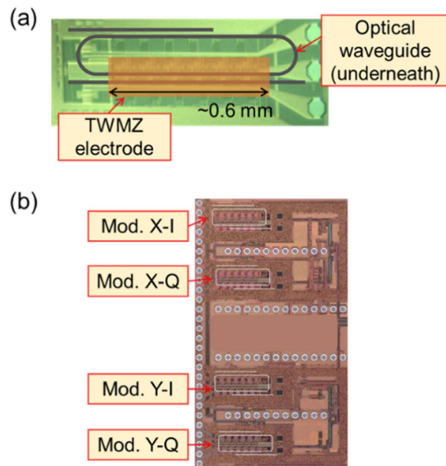


Fig. 5. (a) A micrograph of a fabricated CMRRM and (b) a micrograph of the PIC.

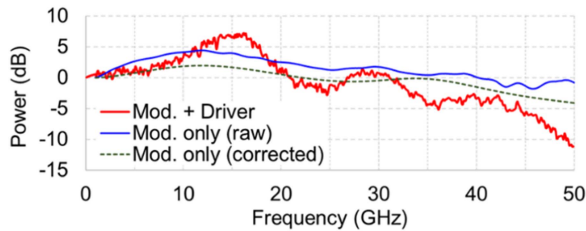


Fig. 6. Measured EO response of one of the four modulators and the combined S21 with the driver and packaging interface.

from resonance, as we did not implement a resonance-locking routine for wafer-level testing. The modulator bandwidth needed to be measured away from the null-bias to detect sufficient signal power. However, this results in additional peaking observed in the raw S21 measurement due to the magnitude of the sidebands that escape the cavity at a given frequency. The amount of peaking depends on the effective coupling coefficient of the embedded TW-MZM when biased off null and how close the sideband frequency is to an integer multiple of the cavity’s free spectral range (FSR). A similar optical peaking effect has been modeled and experimentally observed in conventional cavity-modulated ring resonators when the laser frequency is detuned from resonance [17]. To determine the “intrinsic” bandwidth of the CMRRM (which is fundamentally, the standalone modulator of the TW-MZM bandwidth), we obtain the analytical S21 based on the extracted device parameters [18] and apply a correction to the result to account for both the detunings from null-bias and from resonance. The intrinsic EO response of the modulator is then plotted in dashed green (in Fig. 6). The 3-dB bandwidth, measured on the standalone modulator is ~ 45 GHz. We expect higher bandwidths in future designs by optimizing doping conditions in the pn-junction to reduce the impedance and delay mismatch in the transmission line.

A custom 40-GHz bandwidth, 26-dB gain SiGe BiCMOS driver was developed in-house and optimized for a non-50 Ohm modulator impedance and packaging interface, delivering 4 V peak-to-peak swing with 2% third-order harmonics distortion (THD) and dissipating 730 mW/channel. The driver

has a complete set of features, including gain control, peaking control, peak detectors, and adjustable biasing for the output stage. The combined bandwidth measurement for the driver and the modulator is shown in solid red in Fig. 6. The bandwidth is measured by generating a PRBS signal from an arbitrary waveform generator (AWG) and applying pre-emphasis such that the RF signal is flat at the output of the modulator. The output of the modulator is measured on an optical spectrum analyzer. The measurement is performed with an automatic bias control (ABC) algorithm running, as discussed below. The roll-off due to the cables and mounting substrate board is also measured and normalized out of the result. The combined measured bandwidth is ~ 35 GHz. Even though the driver bandwidth is greater than 40 GHz, the overall device bandwidth is < 40 GHz because the driver design used for this demonstration was optimized for a similar, but different, modulator impedance and packaging interface. Higher BWs can be readily reached with a more finely tuned modulator-driver co-design.

The CMRRMs have an additional bias control compared to the conventional TW-MZMs. Each CMRRM requires two bias controls: one for the TW-MZM (φ_{MZM}) and one for the cavity (φ_{ring}). The φ_{MZM} is for biasing the TW-MZM at null-bias, and the φ_{ring} is for the cavity resonance locking. Thus, for a DP I/Q CMRRM, there are 10 bias controls, compared to 6 for a conventional TW-MZM. We developed a dedicated dither-based ABC algorithm for the module to maintain each modulator’s bias condition and to keep each cavity locked to the input laser wavelength [19]. All module-level bandwidth and data modulation measurements were done with the ABC in operation, i.e., without manual bias control or active temperature control of the setup.

IV. EXPERIMENTAL SETUP FOR THE 800 G FIBER TRANSMISSION

Our experimental setup for the 800 Gbps fiber transmission is shown in Fig. 7. The setup consists of an external cavity laser (ECL), the COSA, and a four-channel 45-GHz arbitrary waveform generator (AWG) (Keysight M8199A) operating at 128 GSa/s. The laser has a linewidth of < 100 kHz and operates at ~ 1550 nm. The AWG output peak-to-peak voltage is set to 500 mV (1 V per pair of differential outputs). We boost the laser power to 21.4 dBm via an EDFA to compensate for the relatively high V_{π} of the modulator as well as for the relatively high losses of our experimental, on-PIC, edge couplers. After data modulation, the modulator output power is -19.3 dBm. The high modulation loss can be addressed by improving the performance of the edge couplers and further reducing the modulator V_{π} s. The modulated signal at the output of the COSA is further amplified by a second EDFA before fiber transmission. The resulting transmitter side OSNR is 34.1 dB. The transmission fiber consists of a single 78-km span of SSMF. The fiber has a loss of 0.2 dB/km and a dispersion of 17 ps/km/nm. The signal is received by a standard discrete components-based DP coherent receiver, consisting of a free-running ECL (~ 1550 nm, ~ 600 MHz away from the transmitter laser), an optical hybrid, four 75-GHz balanced photodetectors (BPDs), and a real-time scope

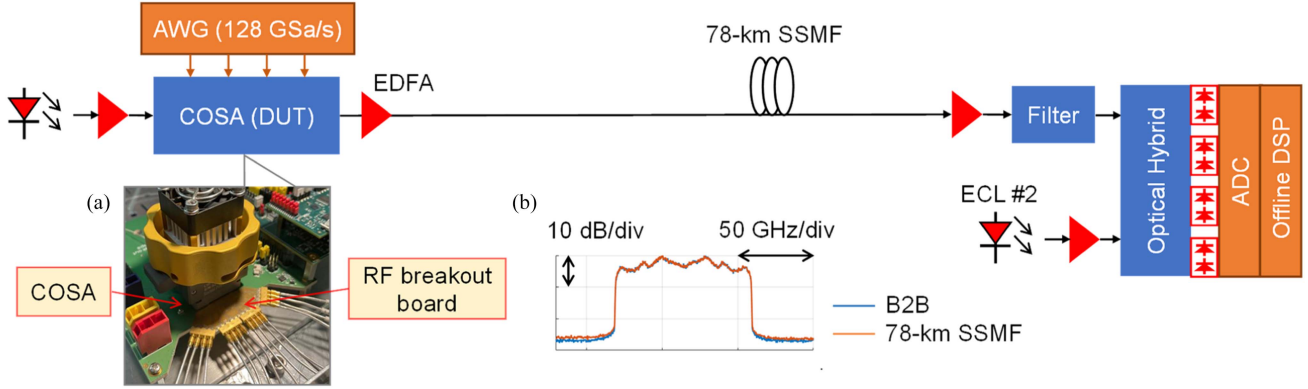


Fig. 7. Experimental setup for the 802.6 Gbps 78-km SSMF transmission with the COSA. Inset (a) shows the COSA mounted on an evaluation board. Inset (b) shows the measured optical spectra before and after the 78-km fiber transmission.

(256-GSa/s with 84-GHz analog bandwidth) with an offline digital signal processor (DSP).

Regarding the modulation format and DSP, we generate a 90-GBaud single carrier signal using root-raised-cosine (RRC) filters which have a 1% spectral roll-off. We use a PS-64-QAM format and adjust the entropy of the symbols to find the highest data rate that yields a normalized generalized mutual information (NGMI) value higher than the threshold required for error-free decoding. Note that in modern modulation and error correction, instead of BER, NGMI is the much more precise figure of merit for predicting post-forward error correction (FEC) performance [20]. To calculate line rate and net rate for PS-QAM, it is necessary to mention the PS-QAM implementation is based on the probabilistic amplitude shaping (PAS) structure where two important parameters, β and γ , describe the shaping. β describes the number of information bits per positive real-valued symbol, and often being referred as ‘constellation shaping factor’. γ describes the number of information bits in the sign of a real-valued symbol and is a function of the QAM template and the FEC code rate (further details can be found in [21]). The line rate R_{Line} and net data rate (information rate) R_{net} can be calculated as follows

$$R_{Line} = N_{pol} \times 2(1 + \beta)r_c \quad (1)$$

where N_{pol} is the number of polarizations, and r_c is the symbol rate.

$$R_{net} = N_{pol} \times 2(\gamma + \beta)r_c \quad (2)$$

There are $\sim 2^{17}$ random symbols used to form each of the transmitter patterns. We use a rate-0.7932 (26.07% overhead) concatenated FEC coding scheme, which consists of a spatially-coupled low-density parity-check (SC-LDPC) rate-0.8 inner code, and a hard-decision Bose-Chaudhuri-Hocquenghem (BCH) rate-0.9915 outer code to remove potential error floors [22]. The required NGMI threshold for error-free decoding is 0.845 [22]. At the receiver, the DSP performs frequency offset compensation, dispersion compensation, frame synchronization, equalization of the waveform via a real-valued 4×4 least mean square (LMS) equalizer operating at 2x oversampling (2SPS), 3rd order Volterra equalization ([16, 16, 16 taps] @ 1SPS), and symbol decision. The Volterra equalizer improves

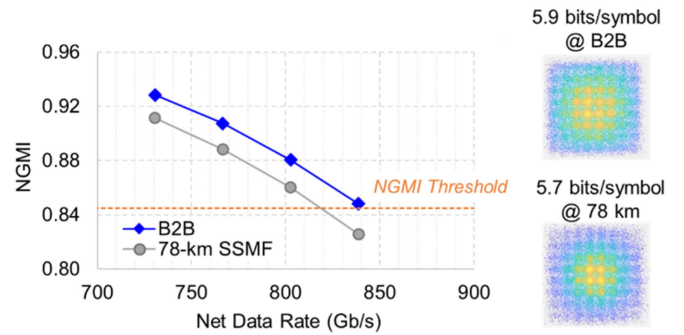


Fig. 8. NGMIs as functions of the net data rate for the 90-GBaud signal for B2B transmission and after transmission through 78-km of SSMF. The insets show the recovered constellations for the B2B and for the fiber transmission.

the SNR by ~ 0.3 dB, mostly mitigating the nonlinearities from the transmitter drivers. The LMS filter has 161 taps (894 ps). About 8,000 symbols are used for pre-convergence, followed by blind equalization. Only the blindly recovered data is used for the NGMI calculation. Roughly 2 million bits are used for the NGMI and BER calculations.

V. RESULTS AND DISCUSSION

The measurement results of the 90-GBaud PS-64-QAM signals are shown in Fig. 8. For the back-to-back (B2B), the measured constellation signal-to-noise ratio (SNR) is 15.4 dB. This allows us to apply constellation shaping factor β of 1.95, meaning an entropy is 5.9 bits/symbol/polarization [21], [22]. The measured NGMI for this constellation is 0.8481 and the BER is 3.9×10^{-2} . For our 64-QAM template and our selected FEC code rate of 0.7932, $\gamma = 0.3796$. Therefore, our achieved B2B line rate is 1.06 Tbps ($2(1 + \beta) \cdot 2pol \cdot 90$ GBaud) and the net data rate is 838.6 Gbps ($2(\gamma + \beta) \cdot 2pol \cdot 90$ GBaud). After transmission through the 78-km fiber, the SNR decreases slightly to 15.1 dB, which allows 5.7 bits/symbol/polarization ($\beta = 1.85$). The measured NGMI is 0.8604 and the BER is 3.6×10^{-2} . The net rate after the transmission is 802.6 Gbps. The insets in Fig. 8 show examples of the recovered PS-64-QAM constellations for B2B (838.6 Gbps) and after 78-km SSMF (802.6 Gbps).

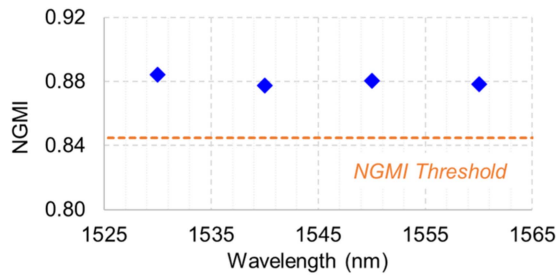


Fig. 9. NGMIs measured (for B2B) at 802.6 Gbps net data rate at various wavelengths in the C-band.

To evaluate the modulator performance on other wavelengths in the C-band, we measure the 802.6 Gbps B2B transmission at various wavelengths across the C-band. The results are shown in Fig. 9. As can be seen, for our COSA, the measured NGMIs as functions of wavelength are very small and above the required threshold.

VI. CONCLUSION

We present an experimental demonstration of a SiPh DP I/Q modulator based on coupling modulated ring resonators for coherent communication in the C-band. The modulators are integrated with SiGe drivers into a COSA. The COSA supports 90-GBaud PS-64-QAM modulation and achieves 832.6 Gbps at B2B transmission and 802.6 Gbps after transmission through 78-km of SSMF. To the best of our knowledge, we believe this to be the first experimental demonstration of a ring-resonator based SiPh DP I/Q modulator for coherent communication with a net data rate greater than 800 Gbps.

REFERENCES

- [1] P. J. Winzer, D. T. Neilson, and A. R. Chraplyvy, "Fiber-optic transmission and networking: The previous 20 and the next 20 years," *Opt. Exp.*, vol. 26, pp. 24190–24239, 2018.
- [2] X. Chen, "Sec 2.3, 'roadmap on optical communications 2023'," *J. Opt. Roadmap*, 2023.
- [3] A. Rahim, A. Hermans, B. Wohlfeil, D. Petousi, B. Kuyken, and D. Van Thourhout, "Taking silicon photonics modulators to a higher performance level ...," *Adv. Photon.*, vol. 3, no. 2, 2021, Art. no. 024003.
- [4] C. Doerr, L. Chen, D. Vermeulen, T. Nielsen, S. Azemati, and S. Stulz, "Single-chip silicon photonics 100-Gb/s coherent transceiver," in *Proc. Opt. Fiber Commun. Conf.*, 2014, Paper Th5C.1.
- [5] P. Dong, X. Liu, S. Chandrasekhar, L. L. Buhl, R. Aroca, and Y.-K. Chen, "Monolithic silicon photonic integrated circuits for compact 100 + Gb/s coherent optical receivers and transmitters," *IEEE J. Sel. Topics Quantum Electron.*, vol. 20, no. 4, pp. 150–157, Jul/Aug. 2014.
- [6] G. Reed, G. Mashanovich, F. Gardes, and D. J. Thomson, "Silicon optical modulators," *Nature Photon.*, vol. 4, pp. 518–526, 2010.
- [7] Nokia Corporation, "Optical Engines." Accessed: May 10, 2024. [Online]. Available: <https://www.nokia.com/networks/optical-networks/#optical-sub-systems/>
- [8] Cisco, "Silicon Photonic Integrated Circuits." Accessed: May 10, 2024. [Online]. Available: <https://acacia-inc.com/product/silicon-photonic-integrated-circuits-pic/>
- [9] R. G. Walker, "High-speed III-V semiconductor intensity modulators," *IEEE J. Quantum Electron.*, vol. 27, no. 3, pp. 654–667, Mar. 1991.
- [10] D. Patel, S. Ghosh, M. Chagnon, A. Samani, V. Veerasubramanian, and M. Osman, "Design, analysis, and transmission system performance of a 41 GHz silicon photonic modulator," *Opt. Exp.*, vol. 23, pp. 14263–14287, 2015.
- [11] P. Dong, L. Chen, and Y. Chen, "High-speed low-voltage single-drive push-pull silicon mach-Zehnder modulators," *Opt. Exp.*, vol. 20, pp. 6163–6169, 2012.
- [12] W. D. Sacher, W. M. J. Green, S. Assefa, T. Barwicz, H. Pan, and S. M. Shank, "Coupling modulation of microrings at rates beyond the linewidth limit," *Opt. Exp.*, vol. 21, pp. 9722–9733, 2013.
- [13] W. D. Sacher, W. M. J. Green, D. M. Gill, S. Assefa, T. Barwicz, and M. Khater, "Binary phase-shift keying by coupling modulation of microrings," *Opt. Exp.*, vol. 22, pp. 20252–20259, 2014.
- [14] A. Mistry, M. Hammood, H. Shoman, S. Lin, L. Chrostowski, and N. A. F. Jaeger, "FSR-free microring-based coupling modulator with integrated contra-directional-couplers," *Proc. SPIE*, vol. 11276, 2020, Art. no. 1127607.
- [15] X. Chen, A. Mistry, M. Bahador, K. Padmaraju, M. Malinowski, and D. Che, "Demonstration of a silicon ring resonator coupling-modulator-based coherent optical sub-assembly operating at 802 Gbps," in *Proc. Eur. Conf. Opt. Commun.*, 2023, Paper M.A.2.5.
- [16] J. Cho, X. Chen, S. Chandrasekhar, and P. Winzer, "On line rates, information rates, and spectral efficiencies in probabilistically shaped QAM systems," *Opt. Exp.*, vol. 26, pp. 9784–9791, 2018.
- [17] J. Müller, F. Merget, S. Sharif, J. Hauck, S. García, and B. Shen, "Optical peaking enhancement in high-speed ring modulators," *Sci. Rep.*, vol. 4, 2014, Art. no. 6310.
- [18] M. Bahadori, Y. Yang, A. E. Hassanien, L. L. Goddard, and S. Gong, "Theory of coupled harmonics and its application to resonant and non-resonant electro-optic modulators," *J. Lightw. Technol.*, vol. 38, no. 20, pp. 5756–5767, Oct. 2020.
- [19] K. Padmaraju, D. F. Logan, T. Shiraishi, J. J. Ackert, A. P. Knights, and K. Bergman, "Wavelength locking and thermally stabilizing microring resonators using dithering signals," *J. Lightw. Technol.*, vol. 32, no. 3, pp. 505–512, Feb. 2014.
- [20] J. Cho, L. Schmalen, and P. J. Winzer, "Normalized generalized mutual information as a forward error correction threshold for probabilistically shaped QAM," in *Proc. Eur. Conf. Opt. Commun.*, 2017, pp. 1–3.
- [21] G. Böcherer, F. Steiner, and P. Schulte, "Bandwidth efficient and rate-matched low-density parity-check coded modulation," *IEEE Trans. Commun.*, vol. 63, no. 12, pp. 4651–4665, Dec. 2015.
- [22] J. Cho and L. Schmalen, "Construction of protographs for large-girth structured LDPC convolutional codes," in *Proc. IEEE Int. Conf. Commun.*, 2015, pp. 4412–4417.